

Journal of
Applied Remote Sensing

RemoteSensing.SPIEDigitalLibrary.org

**Applying persistent scatterer
interferometry for surface
displacement mapping in the Azul
open pit manganese mine (Amazon
region) with TerraSAR-X StripMap
data**

Carolina de Athayde Pinto
Waldir Renato Paradella
José Claudio Mura
Fabio Furlan Gama
Athos Ribeiro dos Santos
Guilherme Gregório Silva
Marcos Eduardo Hartwig

Applying persistent scatterer interferometry for surface displacement mapping in the Azul open pit manganese mine (Amazon region) with TerraSAR-X StripMap data

Carolina de Athayde Pinto, Waldir Renato Paradella,* José Claudio Mura, Fabio Furlan Gama, Athos Ribeiro dos Santos, Guilherme Gregório Silva, and Marcos Eduardo Hartwig

National Institute for Space Research (INPE), São José dos Campos, Avenida dos Astronautas, 1758, PO Box 515, São Paulo State 12227-010, Brazil

Abstract. The Azul mining complex, located in the Carajás Mineral Province, Amazon region, encompasses the most important manganese mine in Brazil. Vale S.A. company operates three simultaneous open pit excavations (mines 1, 2, and 3) in the area, which are conducted on rock alteration products of low geomechanical quality related to sandstones, siltstones, and a lateritic cover. In order to monitor ground deformation, 33 TerraSAR-X (TSX-1) StripMap images covering the period of March 2012–April 2013 were used in the investigation. An advanced differential interferometric synthetic aperture radar (A-DInSAR) approach based on persistent scatterer interferometry (PSI) using an interferometric point target analysis algorithm was applied, and the results showed that most of the area was considered stable during the time span of the synthetic aperture radar acquisitions. However, persistent scatterers (PS) with high deformation rates were mapped over a waste pile, probably related to settlements, and also along the north flank of mine 1, indicative of cut slope movements toward the center of the pit. A spatial relationship of geological structures with PS was observed for this sector of the mine, given by PS showing deformation rates concentrated along a structural corridor with faults, fractures, and folds related to the Carajás fault system. Though only ground-based radar measurements for wall benches of mine 1 were available for a short time period of the TSX-1 coverage, the PS movement patterns showed concordance with geotechnical field measurements. The investigation emphasized the important role that satellite-based A-DInSAR can play for deformation monitoring and risk assessment in this kind of mining area. © The Authors. Published by SPIE under a Creative Commons Attribution 3.0 Unported License. Distribution or reproduction of this work in whole or in part requires full attribution of the original publication, including its DOI. [DOI: [10.1117/1.JRS.9.095978](https://doi.org/10.1117/1.JRS.9.095978)]

Keywords: TerraSAR-X; persistent scatterer interferometry; interferometric point target analysis technique; open pit manganese mine; Carajás Province; Amazon region.

Paper 15569P received Aug. 11, 2015; accepted for publication Nov. 10, 2015; published online Dec. 22, 2015.

1 Introduction

Brazil has 10% of the global manganese (Mn) reserves, after Ukraine (24%), South Africa (22%), and Australia (16%). Vale S.A. is the largest Mn producer in Brazil, accounting for 70% of the country's market. The Azul mining complex (AMC), located along the easternmost border of the Amazon region (Pará State), encompasses the most important Brazilian Mn mine, with a production of 1852 Mt in 2015.¹

Surface deformations potentially lead to slope instabilities due to regular open pit mining operations. The eventual collapse of slopes can cause loss of equipment and risk to personnel, buildings, infrastructures, interruption of production for some mine sectors, and disruption of mining scheduling. This scenario in the AMC gets worse over time due to intense excavations in rock alteration products of very low geomechanical quality, coupled with heavy precipitation of

*Address all correspondence to: Waldir Renato Paradella, E-mail: waldir@tid.inpe.br

the moist tropics. It is worth noting that small surface movements on a mine highwall may be a signal of instability. Thus, a key concern for the mining industry is the prediction of mining-induced deformations of the ground surface.

Most major mines employ geotechnical teams to systematically monitor ground movements, and data on surface stability have traditionally been collected through the use of deformation measurements. A detailed classification scheme of monitoring systems for open pit mines was recently presented,² wherein measurement techniques were divided into surface measurements at discrete points with specific instruments (total stations/reflecting prisms, extensometers, etc.) and surface measurements over areas based on scanning techniques, such as ground-based radar, and image-based techniques. It is important to consider that systems that monitor deformation over large areas yield distinct information when compared to systems designed for monitoring restricted sectors or selected points, because the former can provide valuable data about spatial patterns of deformation. Thus, scanning ground-based radar using differential interferometry, such as slope stability radar (SSR),³ which monitors deformation quasicontinuously, is considered a real-time technique and is widely used by the majority of open pit mines for operational safety. Its rapid response and area coverage are ideal attributes for monitoring slope stability during mining operations, particularly when field accessibility and visibility cannot be guaranteed.

Lower-cost monitoring instruments, such as total station/reflecting prism and extensometer, are normally used for background monitoring of benches/berms, but once instability has been detected, SSR is the instrument of choice by Vale S.A.⁴ However, even though SSR has the ability to cover a broad area, the deformation monitoring is still restricted to sectors of the pit. Since large open pit mining encompasses significant areas with a great demand for land movement information, within and beyond the pit limits (stock and waste piles, tailings ponds, dams, transport routes, processing facilities, mine infrastructure, etc.), the use of differential interferometric synthetic aperture radar (DInSAR) for monitoring purposes is justified, mainly due to the fact of systematic all-weather data acquisition through synthetic aperture radar (SAR) satellite systems are possible. The basic advantages of DInSAR over total station/reflecting prisms or ground-based radar techniques are that measurements of the main spatial movement patterns can be made in the absence of fieldwork and detailed motion information (subcentimeter scale) can be acquired over large areas, rather than point locations or sectors. However, according to Ferretti et al.,⁵ four main problems have limited its operational use: (1) temporal decorrelation of surface scatterers due to surface change processes, (2) spatial decorrelation due to the large baseline between SAR acquisitions, (3) atmospheric effects causing variation in signal delays, and (4) unwrapping phase ambiguity.

In order to overcome the problems of DInSAR mentioned above, advanced DInSAR techniques have presented recent alternatives based on the usage of long time series of interferometric SAR images, which allows millimetric precision ground deformation mapping.⁶ Many successful DInSAR results can be found in the literature related to underground mines,⁷⁻¹⁶ but with few papers concerning open pit mines.¹⁷⁻¹⁹ This paper is an outgrowth of the previous DInSAR investigations carried out with open pit iron mines in the Brazilian Amazon region.²⁰⁻²³ The complexity of the AMC makes the use of DInSAR a challenging application for displacements' monitoring. The mining activities are characterized by excavations on a thick lateritic cover and the dominance of rock alteration masses showing low geomechanical quality, by heavy rainfall periods, and highly dynamic surface changes due to constant reworking and removal of materials, all contributing to an overall loss of radar coherence. In this paper, we report the results of the application of persistent scatterer interferometry (PSI) for mapping ground displacements in the AMC using TerraSAR-X (TSX-1) data.

2 Test Site

The Azul deposit (shown in Fig. 1) was discovered in September 1971 and the mining activities started in 1985, with reserves of 45.4 Mt at 40.5% proven and 8.3 Mt at 39.5% probable (December 2011). This deposit is recognized internationally for the excellent quality of its ore, which contains high concentrations of Mn and a high Mn-Fe ratio. Today, the total

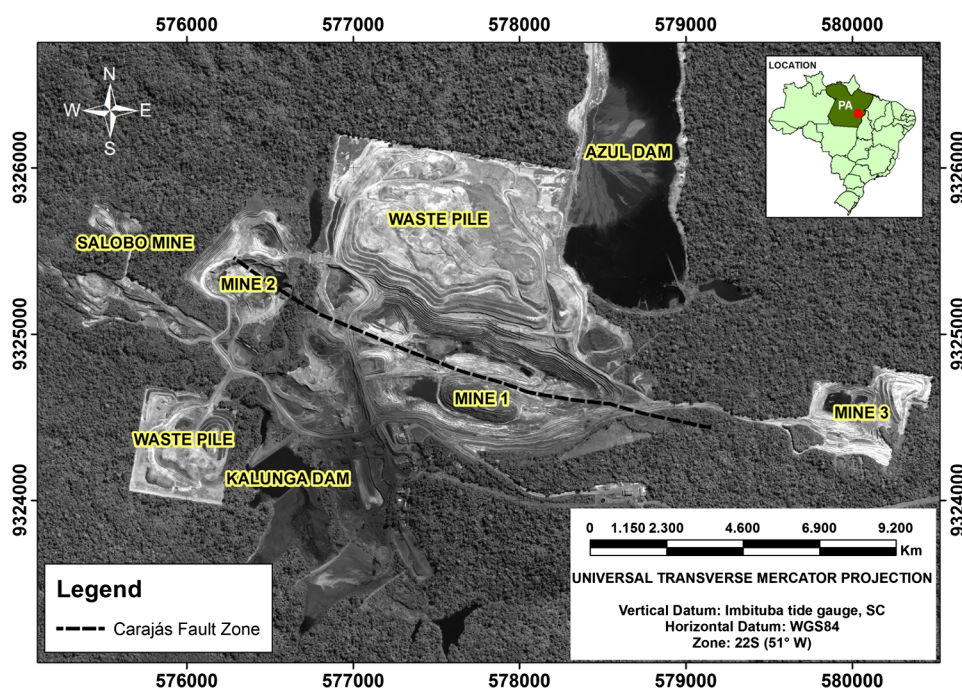


Fig. 1 Azul mining complex with three simultaneous active open pits (mines 1, 2, and 3), two waste piles, and mining infrastructure.

area of AMC is $\sim 2.5 \text{ km}^2$, spanning three open pits (mines 1, 2, and 3) and a processing plant. The AMC presents excavations reaching a total height of 80 m, with 4 to 8 m bench height and 5 m berm width. A large waste pile is located along the northern border of mine 1 (waste pile north). It is a mining structure with 20 years old, with a heaped-fill dump configuration, with 10 m bench height, 10 m berm width, and 27 deg of overall slope angle (crest-to-toe).

The Azul deposit is related to the Proterozoic Águas Claras formation, which is characterized by a progradational succession of platform sediments in the lower part and littoral and fluvial deposits in the upper part.²⁴ The primary mineralization is hosted in a pelitic sequence on the basal portion of this unit (Azul member); and the secondary mineralization, which is considered the most important ore, is related to residual/supergene enrichment associated with a mature lateritic toposequence acting from at least the Upper Cretaceous throughout the Tertiary and Quaternary. The geologic sections exposed in the mining area show the presence of siltstones/pelites, fine red to white sandstones, and lens-formed layers made of gray siltstones to gray black shales, rich in carbonaceous organic matter and/or Mn oxi-hydroxides or rhodocrosite, characteristics of terrigenous/chemical and lateritic sources. Primary structures such as hummocky cross stratification and parallel laminations are common in these rocks. Bedding with a thickness of centimeters to a few meters (30 to 50 cm) represents the main primary structure. The lateritic profile is deep (100 m) and is characterized by differentiated horizons, which correspond to progressively upward physico-chemical degradation from a thick clayey horizon to nodular lateritic crust, breccia-like, cavernous, or massive. Large sectors of the mining area are covered by yellowish brown earthy to clayey material, with spheruliths concentrated at the base as a product of chemical and physical weathering of the lateritic profile, and deposited by gravity in paleodepressions or paleovalleys.²⁵

Structurally, the Azul deposit is located in the central portion of the Carajás Strike-Slip System (CSSS) with rocks organized in asymmetric folds cut by E-W trending directional/thrust faults and N-S trending normal faults, partitioned in different scales. The parallelism of the structural trends in the mining area and lineaments related to the CSSS suggests a close relation with regional deformations (dextral transtensional and sinistral transpressional episodes). Faults with normal kinematics associated with the dextral component of displacement are the major exposures in the area and are interpreted as related to the transtensional episode of the installation of the Carajás fault prior to 2.6 Ga. Folds, thrust faults, and subvertical fault zones would be related

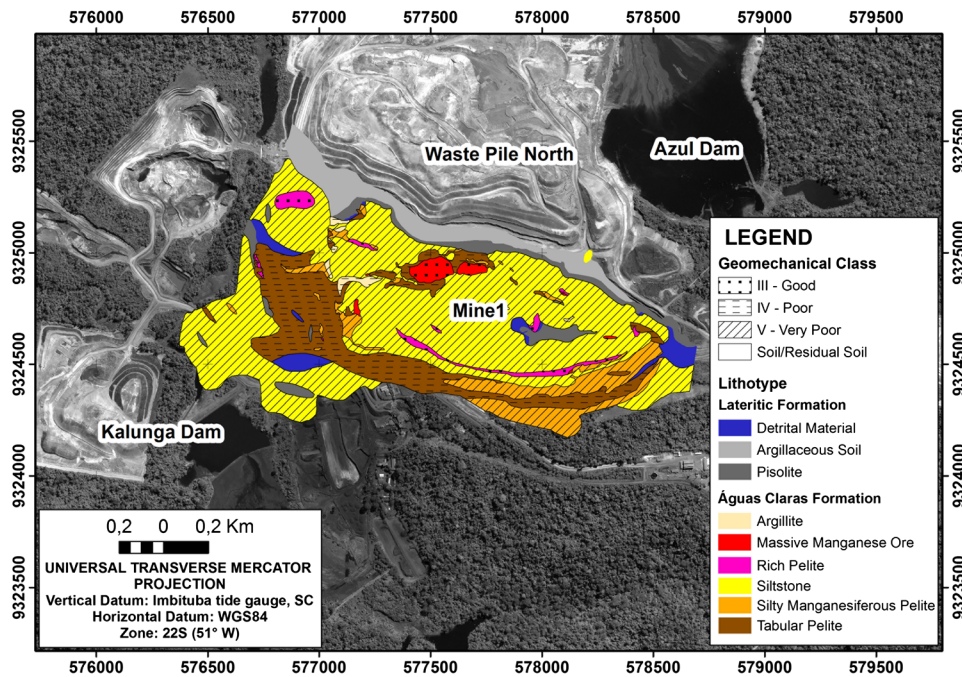


Fig. 2 Lithological and geomechanical units in mine 1.

to deformation under the sinistral transpressional regime, a second event responsible for the reactivation and tectonic inversion of most of the primary structures near the Carajás fault zone.²⁶

According to Silva,²⁷ the Azul mine is divided into two blocks separated by a NW to EW trending normal fault, representing a trace of the Carajás fault. A large (~700 m) vertical displacement between the two adjacent blocks was predicted based on offsets in the stratigraphy of the Águas Claras formation with the northern block uplifted relative to the southern one. The southern block is poorly deformed, with irregularities in bedding which dips at shallow angles toward the south. In the northern block, bedding shows a heterogeneous behavior. Deformation is more expressive in this block, with the ore deformed by folds and reverse faults. Faults show vertically along dipping kinematics with dextral conjugated displacements of oblique character. This sector can be defined as a major strain corridor.

The most detailed available account of the geological and geomechanical information for the Azul mine was produced by Vale's geotechnical team,²⁸ including surface outcrop mapping at a 1:2000 scale, classification of rock types based on standard mining nomenclature, characterization of structural and geomechanical parameters, and definition of lithostructural domains restricted for the slopes of mine 1. Furthermore, a slope stability analysis was also carried out, which involved the collection of structural data, slope geometry, and subsequent limit equilibrium analysis in order to characterize the conditioning structures of slope ruptures. Based on this report, rock types and alteration products are characterized with variations in the degree of weathering and strength, but with a dominance of types of poor mechanical properties. The integration of geological and geomechanical information is presented in Fig. 2. Based on the field mining nomenclature, the lithotypes were classified as siltstones, argillites, silty manganiferous pelites, massive Mn ore, and rich Mn content pelites and pisolites. A lateritic detritic cover and argillaceous soil are also common. The geotechnical quality of the rock masses was evaluated based on rock mass rating parameters;²⁹ and poor and very poor classes are dominant, while good rock masses crop out as isolated bodies. Two main structural features were mapped in mine 1 (notation dip direction/dip): (1) beddings with two dominant attitudes (36/207 and 43/016) and (2) fractures/faults with four attitude systems (71/43, 69/129, 67/224, and 68/311). Finally, the kinematic analysis has pointed out the possibilities of distinct failures (plane, wedge, circular, and toppling) along sectors of cut slopes of mine 1. Since the detailed information is concentrated around mine 1, the PSI analysis was restricted to this sector of the AMC.

3 Dataset

A stack with 33 TSX-1 StripMap images (repeat cycle of 11 days) was used in this investigation. Conflicts in acquisition programming of the satellite caused four interruptions in the original one-year acquisition coverage starting on March 20, 2012, with four interruptions in 2012 (December 31) and 2013 (February 13, February 24, and March 7). The single look complex (SLC) images were acquired under ascending passes (look azimuth = 78 deg), incidence angle range of 39.89 to 42.21 deg, spatial resolution of 1.7 m \times 3.49 m (rg \times az), pixel spacing of 1.36 m \times 1.90 m (rg \times az), and width swath of 30 km. In order to minimize the topography phase error in the interferometric process, a high-resolution digital elevation model (DEM) was produced based on a panchromatic GeoEye-1 stereo pair. The GeoEye-1 stereo images were acquired over the study area on July 1, 2012. The first scene was collected with nominal azimuth and elevation angles of 29.4 and 82.4 deg, respectively, whereas the second scene was acquired with azimuth and elevation angles of 187.42 and 62.20 deg, respectively. The images were provided with 0.5 m spatial resolution and with rational polynomial coefficients. The generation of the DEM was based on OrthoEngine PCI Geomatics through the rational function method as the geometric model. The DEM was produced at 2 m spacing using one ground control point and its values were compared to seven accurate vertical check points, and the RMS and maximum errors of 1.2 and 1.6 m, were obtained.³⁰

The slope monitoring scheme used in the region includes regular visual inspections to detect the onset of instability and instruments measuring surface (total station/reflecting prisms and ground-based radar) and subsurface displacements (piezometers and extensometers). Only information produced from the ground-based radar SSR was available for this investigation.³¹ Ground-based differential interferometry employs phase values from two radar scans targeting the same area, producing an interferogram. The interferogram is then subtracted from an earlier or original scan to measure any displacement that might have taken place. So by taking the phase value of a single radar return and comparing the information with phase information from a different scan of the same target, an accurate depiction of the slope activity can be achieved. SSR is featured by a 1.80-m-diameter scanning parabolic dish antenna, mounts, controlling/data-collecting computer, remote area power supply, warning siren and lights, CCD camera, communication links, and Internet compatibility. The system uses real aperture radar to scan a slope both vertically (height) and horizontally (azimuth) with a scanning at a rate of 10 deg/s over a range of ± 60 deg vertically and 270 deg horizontally. The typical scan repeat time is 15 min. Line of sight (LOS) displacement can be measured to ± 0.2 mm without the use of reflectors. For the configuration used in the Azul mine, the SSR pixel size was ~ 1.7 m \times 1.7 m. The SSR data corresponded to measurements taken on bench walls located along the southern flank of mine 1 and covered a short time span (August 3 to August 8, 2012). A small deformation pattern was detected, which was not considered relevant enough to cause significant ruptures in the slopes.

4 Methodological Approach

The pluviometric record available for the mining complex during the TSX-1 passes has indicated a total of 3149 mm for the accumulated precipitation (Fig. 3). The dry season encompassed the interval from the end of March 2012 up to the beginning of October 2012, whereas the rainy season covered the period from October 2012 up to April 2013. Taking into account these values and the probable influence of rainfall in the SAR coherence, the PSI analysis was conducted in two stages: a first step using the first 19 TSX-1 images related to the dry season (March 20 to October 4, 2012) and a second step based on the last 15 TSX-1 scenes covering the wet season (October 4, 2012 to April 20, 2013).

The PSI approach study relies on identifying pixels for which scattering properties vary little with time and look angle in a stack of coregistered SLC images. These point-likely targets or so-called persistent scatterers (PS) are coherent even for the interferometric pairs with long spatial baselines and remain stable to permit analysis of the phase history.^{32–34} PSI analysis was carried out using interferometric point target analysis (IPTA) software, which is the implementation of PSI by GAMMA Remote Sensing and Consulting AG (GAMMA). The IPTA software is a toolbox that can support many different methodologies, including different alternatives for PS

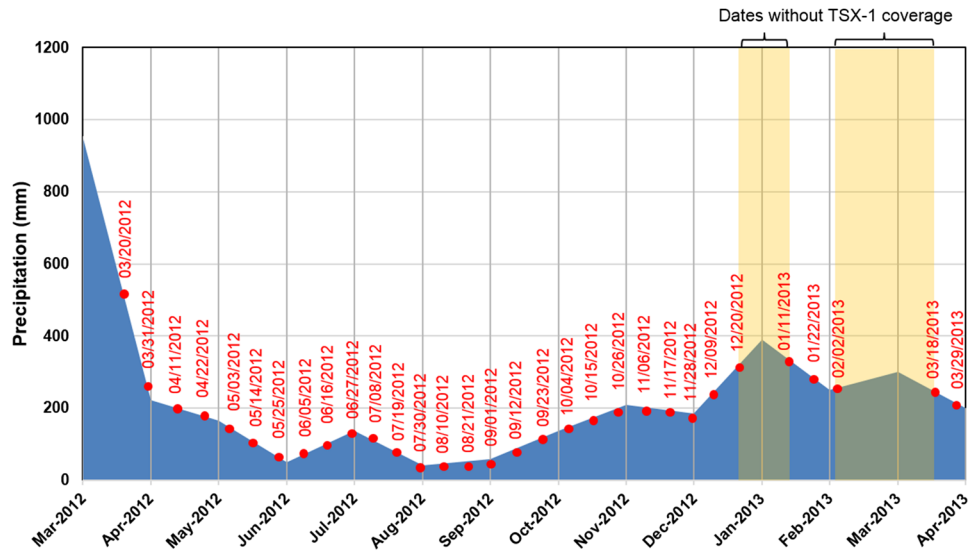


Fig. 3 Precipitation values (blue) and dates of the TerraSAR-X (TSX-1) acquisitions (red) in the study area.

candidate selection, spatial and temporal phase unwrapping, and supporting approaches for single- as well as multireference stacks.³⁵ The overall processing using IPTA is depicted in Fig. 4. The processing sequence included SAR SLC image coregistration to generate the stack of interferograms (the master scene was selected based on a configuration that has low perpendicular baseline dispersion and is near to the center of the image sequence, Table 1), stack of differential interferograms generation, point target candidate determination (based on spectral phase diversity and low-intensity variability), interferometric point analysis based on two-dimensional regression (phase model indicates a linear dependence of the topographic phase on the perpendicular baseline and also a linear time dependence for deformation rates), and model refinement (update the DEM, update deformation rates, baseline refinement).

An important aspect of IPTA is the possibility of a step-wise, iterative improvement for different parameters, such as the topographic error based on a linear regression with the perpendicular baseline set and the linear regression for deformation estimation. The residues

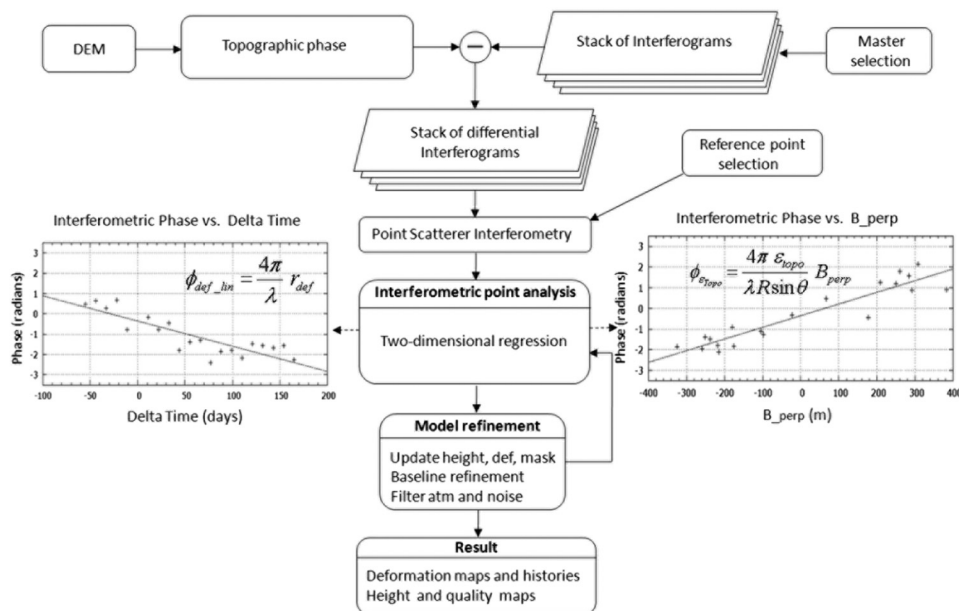


Fig. 4 Flow diagram outlining the interferometric point target analysis processing sequence.

Table 1 Differential Interferometric TerraSAR-X (TSX-1) images used in the persistent scatterer interferometry processing for dry and wet seasons.

Master	Slave	Perpendicular baseline (m)	Temporal baseline (days)
	March 20, 2012	79.39	-110
	March 31, 2012	-82.80	-99
	April 11, 2012	-140.96	-88
	April 22, 2012	411.41	-77
	May 3, 2012	-119.80	-66
	May 14, 2012	98.88	-55
	May 25, 2012	386.88	-44
	June 5, 2012	-6.547	-33
	June 16, 2012	-228.91	-22
	June 27, 2012	487.23	-11
July 8, 2012	July 8, 2012	0	0
	July 19, 2012	-163.87	11
	July 30, 2012	279.61	22
	August 10, 2012	394.86	33
	August 21, 2012	-120.72	44
	September 1, 2012	-78.20	55
	September 12, 2012	-154.28	66
	September 23, 2012	309.99	77
	October 4, 2012	166.72	88
	10/04/2012	-57.61	-77
	October 15, 2012	138.63	-66
	October 26, 2012	128.26	-55
	November 6, 2012	-426.57	-44
	November 1, 2012	-3.60	-33
	November 28, 2012	-119.21	-22
	December 9, 2012	-147.39	-11
December 20, 2012	December 20, 2012	0	0
	January 11, 2013	-201.40	22
	January 22, 2013	-335.31	33
	February 2, 2013	-155.96	44
	March 18, 2013	-151.17	88
	March 29, 2013	68.69	99
	April 9, 2013	111.99	110
	April 20, 2013	-30.06	121

of this last regression containing the atmospheric phase, which is related to the path delay heterogeneity at the two acquisition times of the pair, as well as nonlinear deformation and noise, were filtered spatially and in time to decrease the atmospheric phase delay and noise as well as retrieve the nonlinear deformation component. The following information can be retrieved: geographic coordinates of the PS (latitude, longitude, and elevation), time-series of displacement values (mm), and average displacement rate (mm/year). All the displacements are the projection along the satellite LOS of the three-dimensional displacement vector affecting the target. These are differential measurements with respect to a reference point selected within the area of interest and assumed as stable and time referenced to the acquisition date of the first scene. Therefore, displacements data provided for PS are relative, not absolute data. An important parameter for precision accuracy can be estimated through the dispersion of PS values regarding the reference point expressed by the standard deviation of the velocity rate, which can be represented according to GAMMA (Ref. 36) by

$$\sigma_{Vd(x,r)} = \sqrt{\sum_{i=1}^N \left(\frac{\lambda}{\Delta t_i 4\pi} \Delta \phi_i - \frac{\lambda}{4\pi} \phi_{\text{rate}} \Delta t_i \right)^2 / \Delta t_i^2}, \quad (1)$$

where

$$\phi_{\text{rate}} = \frac{\sum_{i=1}^N \Delta t_i \Delta \phi_i}{\sum_{i=1}^N \Delta t_i^2}. \quad (2)$$

$\Delta \phi_i$ is the phase displacement during the time interval Δt_i and N is the number of interferograms.

5 Results and Discussions

PS were detected and deformations were expressed by time-series of displacement and average displacement rate values in the World Geodetic System 84 coordinates relative to a reference point assumed to be stable (location: 577,255.375E; 932,4042N). Positive values correspond to motion toward the satellite, whereas negative values correspond to motion away from the satellite. The IPTA analysis for the dry season has allowed the detection of 40,193 PS in an area of 2.5 km², with an average density of ~8588 PS/km². Using the data stack for the wet season allowed the detection of 20,577 PS, with an average density of ~4680 PS/km². The deformation maps for both periods can be seen in Fig. 5.

The distribution of PS was not homogeneous: no stable targets were present on vegetated areas (low coherence), while the detection of points was very good over the mining areas (within and beyond the pit limits, waste piles, processing facilities, and related infrastructure). IPTA results provided a unique view of the ongoing deformative process in the mining area and showed that most of the area was stable during the time span of the TSX-1 coverage (yellow-greenish regions in maps of Fig. 5). The most intense displacements were related to PS located over the north waste pile (reddish sectors, letters A and C in Fig. 5), reaching maximum accumulated displacements of -8.65 cm (dry season) and -6.25 cm (wet season) and displacement rates of -17.02 cm/year (dry season) and -14.50 cm/year (wet season), respectively. These motions are indicative of subsidence and are interpreted as settlements.

Waste material settlements occur due to several causes such as particle reorientation, weathering of high clay-content materials, presence of water in interparticle bounding, and transport of particles through the dump. During construction, a higher settlement rate may occur followed by lower vertical deformation at a decreasing rate, which has been shown to continue 10 years or more after the pile construction. The rate of settlements of waste dumps is a controversial issue in the literature, since it depends on several parameters (dump height, dump type, loading rate, type of material, dump construction time, etc.), with large variations of settlements (0.3 up to 20%) regarding the waste dump height being reported;³⁷ but in general, vertical settlements of a few meters are normally expected according to Vale. Thus, the LOS accumulated values expressing subsidence are within the expected limits. Furthermore, it is also important to mention that

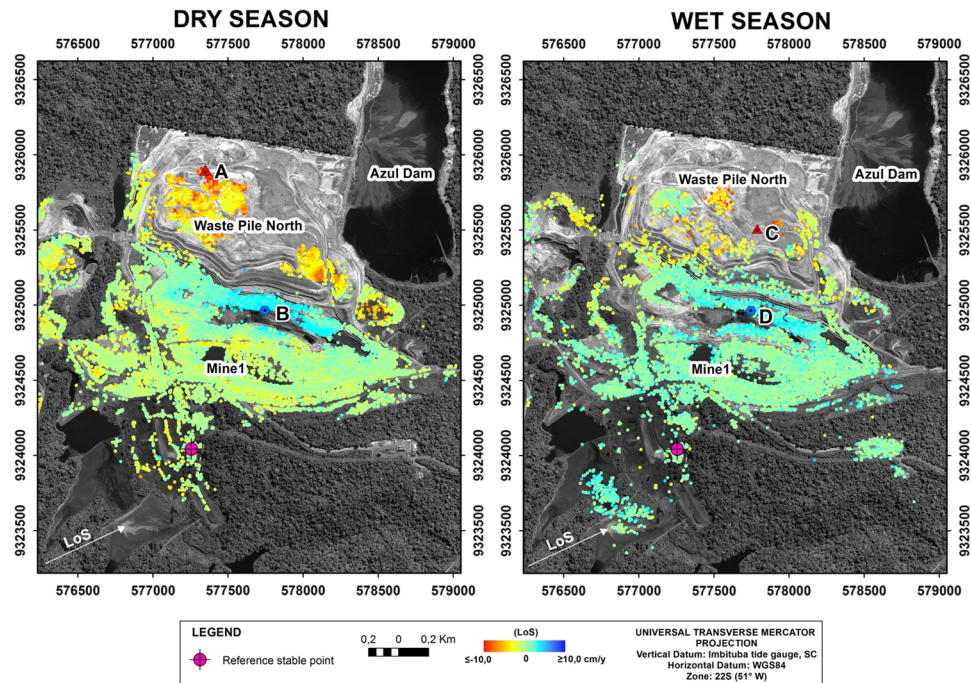


Fig. 5 Spatial distribution of persistent scatterers (PS) for mine 1 and north waste pile, visualized by the average line of sight (LOS) velocity on the panchromatic GeoEye-1 scene for dry and wet seasons. Letters A, B, C, and D are discussed in the text.

sectors of ground displacements were not detected with positive values characterized by bulging at the dump toe indicative of pile instabilities. Finally, it is also clear, by the overall absence of PS within sectors of the pile, that this manmade structure has suffered intense surface changes due to ongoing mining operation, expressed by the low coherence.

For the remainder of the mining area, ground displacements were also detected for cut slopes along the northern flank of pit 1 with positive values indicative of movement toward the satellite (bluish regions, letters B and D in Fig. 5), with values for maximum accumulated displacement of 2.41 cm (dry season) and 3.95 cm (wet season) and displacement rates of 4.67 cm/year (dry season) and 6.23 cm/year (wet season). These slopes are related to highly weathered siltstones of the Águas Claras formation with low geomechanical attribute (rock mass rating/class V). The deformation profiles for the discussed PS are presented in Fig. 6. The accuracy of the detected deformation rates can be evaluated by their estimated deformation rate uncertainties, which were 0.24 and 1.69 cm/year for dry and wet seasons, respectively. It is important to consider that a change of elevation at any location on a mining bench is a result of two components: the vertical movement (subsidence) and the horizontal shift of the ground. If these two movements act on a mining bench, and the horizontal component is oriented toward the center of a pit, the result can be an apparent heave of the ground (apparent uplift).³⁸ Under an ArcGIS environment, the information from IPTA and geomechanical maps for mine 1 was compared in order to explore spatial relationships. Table 2 reveals that the highest amount of PS was associated with the geomechanical classes of the largest areas, but showing the lowest densities (classes IV, soil/residual soil). These two classes, and also class V, present geomechanical attributes of poor quality, and also with the most intense exploitation activities (siltstone). In addition, the results of IPTA processing comparing wet with dry seasons have shown that a total of 13,685 PS was lost, with losses for all classes.

Tables 3 and 4 provide quantitative stability results considering specifically the north and south flanks of mine 1 (Fig. 7) and assuming three distinct intervals of accumulated displacements: (1) indicative of motion away from the satellite (< -0.5 cm), (2) indicative of stability (≤ 0.5 cm up to ≥ -0.5 cm), and (3) indicative of motion toward the satellite (> 0.5 cm). The intervals were chosen taking into account that ± 0.5 cm was the standard deviation (1σ) obtained over a stable surface (reference).

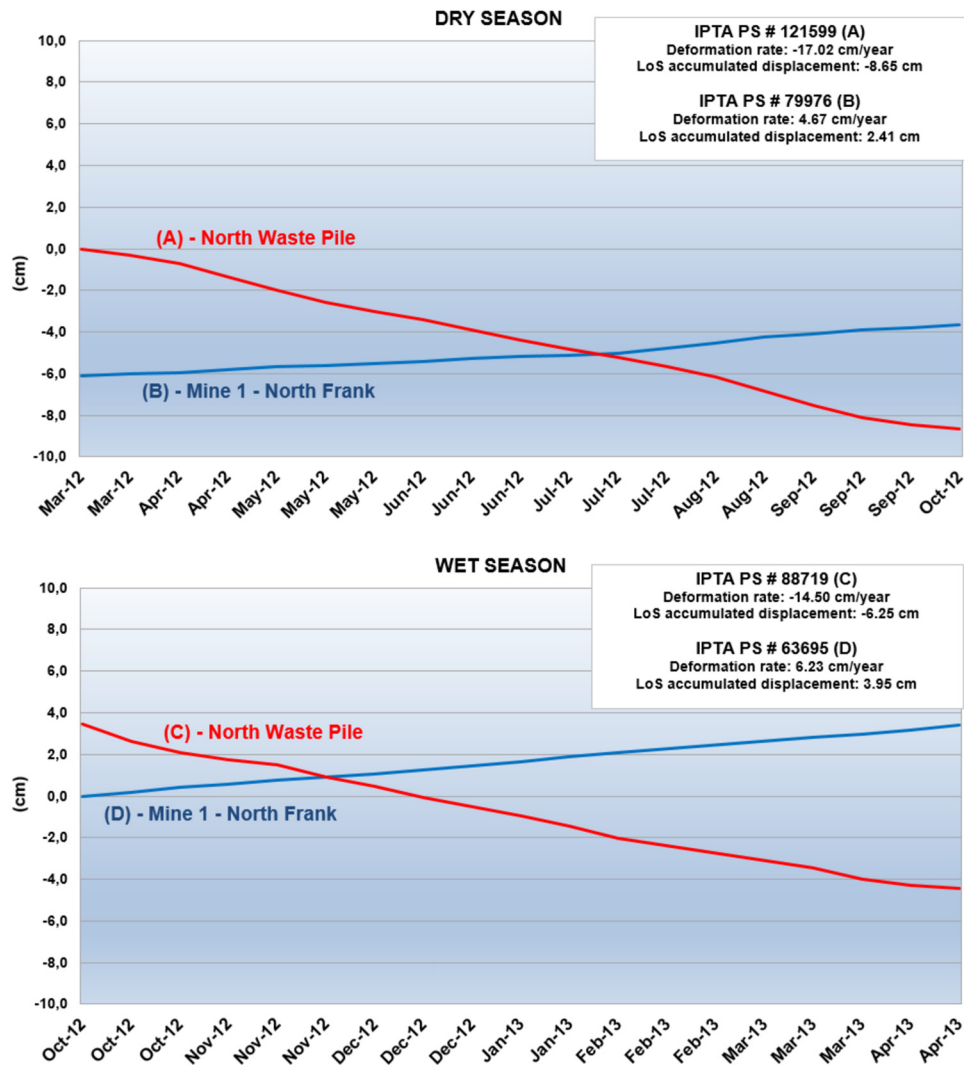


Fig. 6 Temporal evolution of the LOS-projected deformation for PS located within the north waste pile (red profiles, letters A and C) and along the cut slope of the northern flank of mine 1 (blue profiles, letters B and D) for dry and wet seasons.

For the northern flank, when IPTA results for wet and dry seasons were compared (Table 3), a total of 1935 PS (45.7%) was lost considering all geomechanical classes, and a new spatial distribution of PS was obtained. Rainfall is considered to be the main cause for the loss of temporal coherence with a lower number of detected PS. In addition, for both periods, a large dominance of PS with positive values expressing a movement toward the satellite was noted. On the other hand, IPTA results for the southern flank (Table 4) also indicated a loss of PS (~30%) when

Table 2 Relationship between persistent scatterers (PS) and geomechanical classes for mine 1.

Geomechanical class	Area (km ²)	Dry season		Rainy season	
		Number of PS	PS/km ²	Number of PS	PS/km ²
III (good rock)	0.06	1133	18,883	670	11,167
IV (poor rock)	0.53	5701	10,757	2757	5202
V (very poor rock)	1.38	20,962	15,190	12,208	8846
Soil/residual soil	0.54	4238	7848	2714	5026

Table 3 Relationship between deformation and geomechanical classes (northern flank).

Geomechanical class	Dry season				Rainy season			
	Total of PS	PS with displacements indicative of stability (%)	PS with displacements toward the satellite (%)	PS with displacements away from the satellite (%)	Total of PS	PS with displacements indicative of stability (%)	PS with displacements toward the satellite (%)	PS with displacements away from the satellite (%)
III	20	0	100	0	0	0	0	0
IV	123	4	96	0	132	11	83	6
V	1908	0	98	2	732	11	86	3
Soil	1513	9	89	2	765	20	72	8

Table 4 Relationship between deformation and geomechanical classes (southern flank).

Geomechanical class	Dry season				Rainy season			
	Total of PS	PS with displacements indicative of stability (%)	PS with displacements toward the satellite (%)	PS with displacements away from the satellite (%)	Total of PS	PS with displacements indicative of stability (%)	PS with displacements toward the satellite (%)	PS with displacements away from the satellite (%)
III	642	75	15	10	0	0	0	0
IV	1325	28	1	71	996	30	5	65
V	4422	41	4	55	3517	33	6	61
Soil	136	50	4	46	19	31	6	63

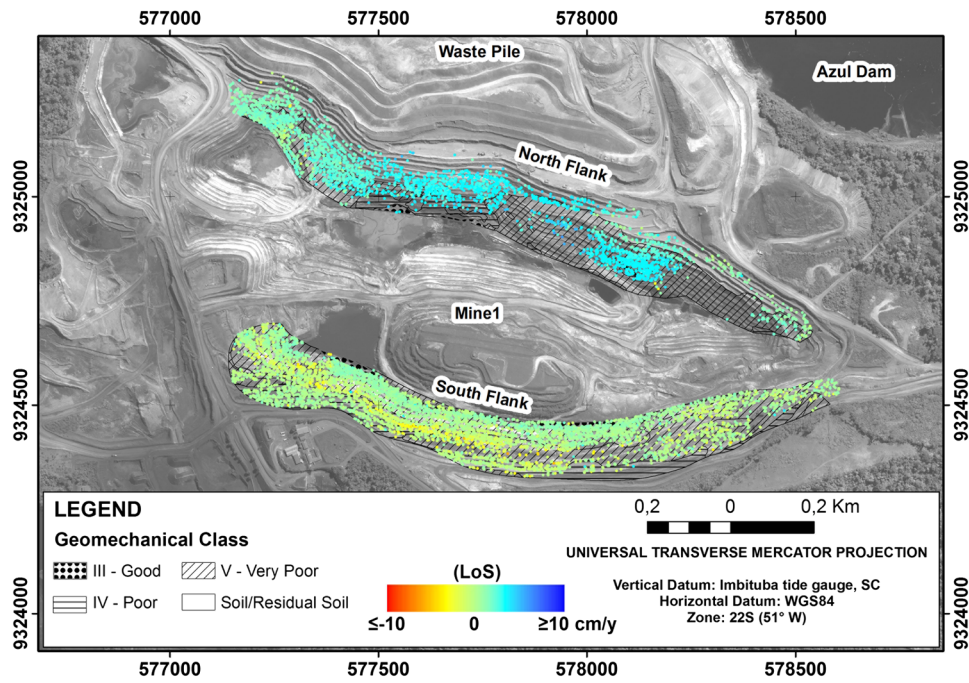


Fig. 7 Spatial distribution of PS (dry season) and geological/geomechanical classes for the north and south flanks of mine 1.

comparing wet with dry seasons, but with a dominance of PS with smaller negative values indicative of motion away from the satellite. Finally, a higher number of PS expressing stability were detected for the southern as compared to the northern flank, and the combination of positive and negative values for both flanks is indicative of movements toward the center of the pit.

It is important to mention that the deformation was more expressive along the northern block of the kilometer-scale structural corridor (region A, Fig. 8), with PS mainly located along the trace oriented to the NW-SE of the Carajás fault system, indicating considerable strain on the cut slopes. The southern block of mine 1 is poorly deformed (region B, Fig. 8), with bedding predominantly oriented to E-W and dipping toward south. In this region, it can be seen that the PS

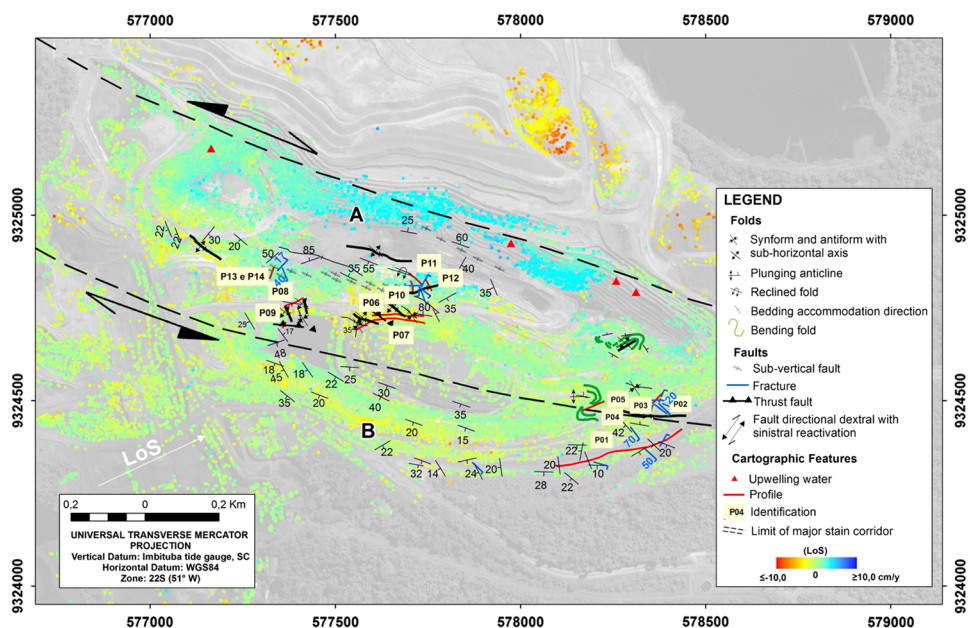


Fig. 8 PS distribution (dry season) and structures in mine 1 (geological source from Ref. 27).

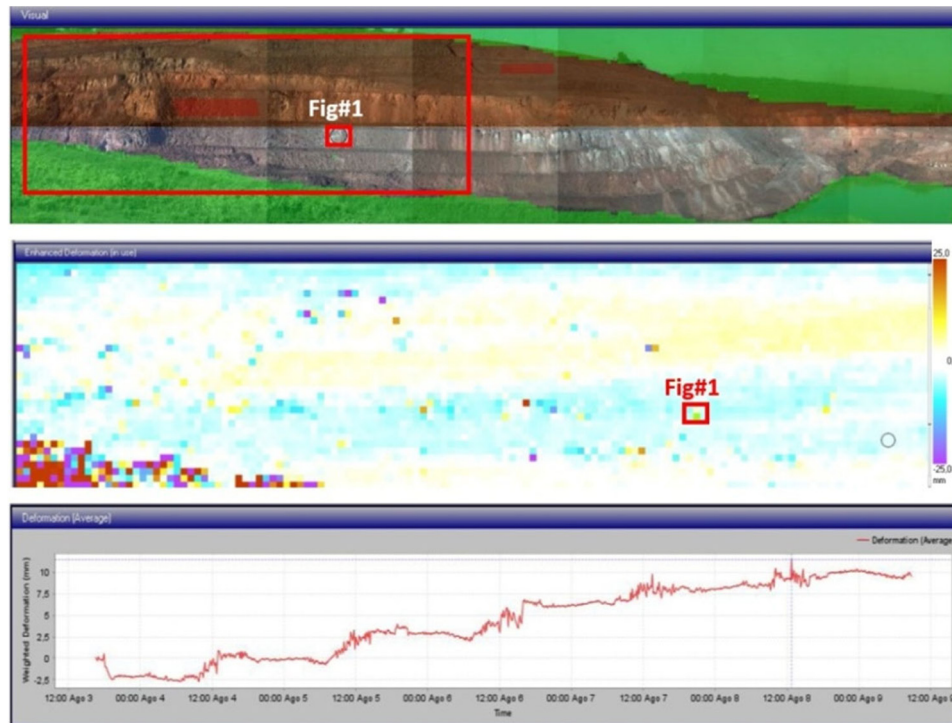


Fig. 9 LOS-projected slope stability radar (SSR) deformation plot showing (a) the photograph of the scanned area (top) and (b) corresponding heat map deformation of the scanned area. The color scale (purple to red) represents lower to higher LOS-projected SSR displacement variation (middle). (c) Deformation profile for the selected area (red small rectangle) showing small collapses followed by stabilization (bottom).

distribution did not have significant deformation rates, indicative of slope stability during the TSX-1 coverage. The second sinistral transpression event that affected the rocks exposed in the Azul mine generated a sequence of structures (normal faults, flexural folds, etc.) mapped in the field through geologic sections (profiles P01 to P14, Fig. 8). PS values near these profiles are indicative of stability for dry and wet seasons (yellow-greenish colors), with the exception of P11 and P12, which are related to areas of higher deformation rates indicative of displacements with positive values (green-bluish colors). These two profiles are located in the middle of the major strain corridor, where deformation is more intense, characterized by folded bedding (drag folds), fractures, and a complex set of faults, with distinct orientations (N-S, NE-SW, NW-SE) displaying normal and uncertain shear senses.²⁷ Finally, few PS in the eastern portion of the northern flank can be seen (red triangle, Fig. 8). According to an internal Vale's report, this particular sector is characterized by the presence of upwelling water sources that cause loss of radar coherence and, consequently, reduce the PS detection.

In an attempt to validate the IPTA results with field information, SSR measurements were used. Unfortunately, only SSR data for a small sector of the southern flank were available during the TSX-1 coverage. Despite the short monitoring period (August 3 up to August 8, 2012), a small deformation pattern was detected, given by successive small collapses followed by stabilizations, with a maximum accumulated LOS-projected SSR deformation value of 15 mm (Fig. 9).

In order to explore spatial relationships, the distinct viewing geometries for SSR and TSX-1 were superimposed on the panchromatic GeoEye-1 orthoimage (Fig. 10). It can be seen in this figure that the look directions for both imaging radars (orbital and ground-based) are almost orthogonal. Thus, the measured motion component along the SSR LOS would be attenuated when projected to the TSX-1 LOS, since no significant phase variation is detected if the terrain is affected by displacements in the direction perpendicular to the sensor LOS. The LOS-projected TSX-1 deformation profiles for three points (A, B, and C, Fig. 10), specially located along the SSR look azimuth (from bottom to the top) of the benches of the south flank,

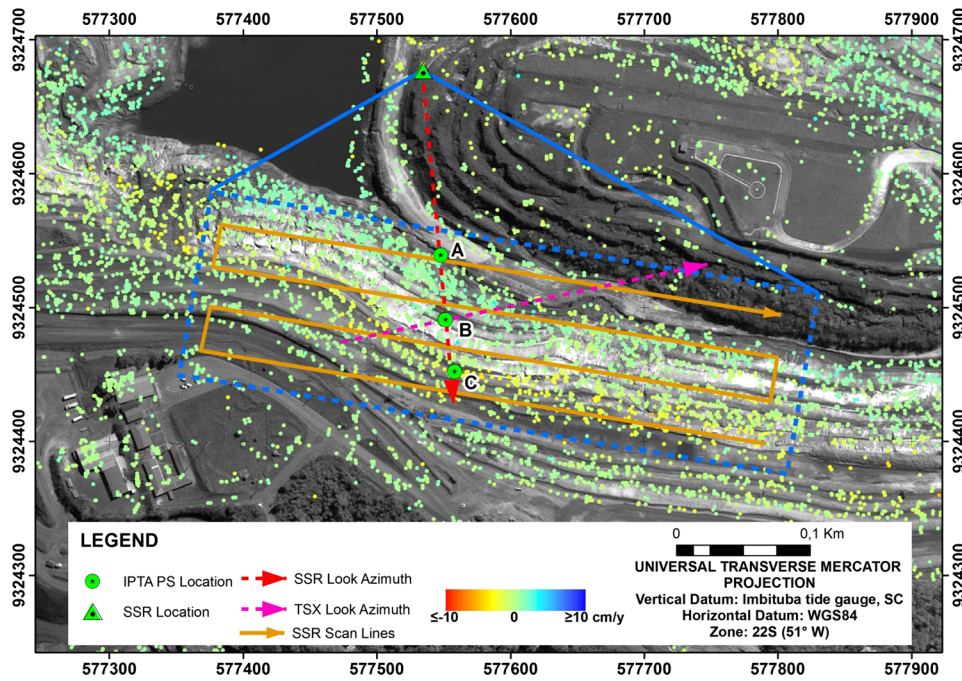


Fig. 10 Scheme of viewing geometries used by TSX-1 and by SSR during the monitoring of bench walls along the southern slopes of pit 1. Legend: TSX look azimuth (magenta), SSR look azimuth (red), SSR location (green triangle), points A, B, and C along SSR look azimuth are discussed in the text. Point B corresponds to the same location where the SSR deformation plot was produced.

were analyzed. The PS profiles (Fig. 11) revealed the presence of slope displacements with negative values (away from the satellite) with small rates, increasing from the bottom to the top of the benches (point A = -0.37 cm/year, point B = -0.70 cm/year, and point C = -4.21 cm/year). Point B is almost in the same location, where the SSR profile was acquired with a total accumulated displacement of 15 mm for the six-day monitoring period. The direct comparison of deformation values measured by both systems is not feasible due to distinct aspects (sensor viewing geometry, bench faces measurement with SSR and benches/berms with TSX-1, time-scan, etc.). However, they are concordant regarding the presence of small movements along the cut slopes.

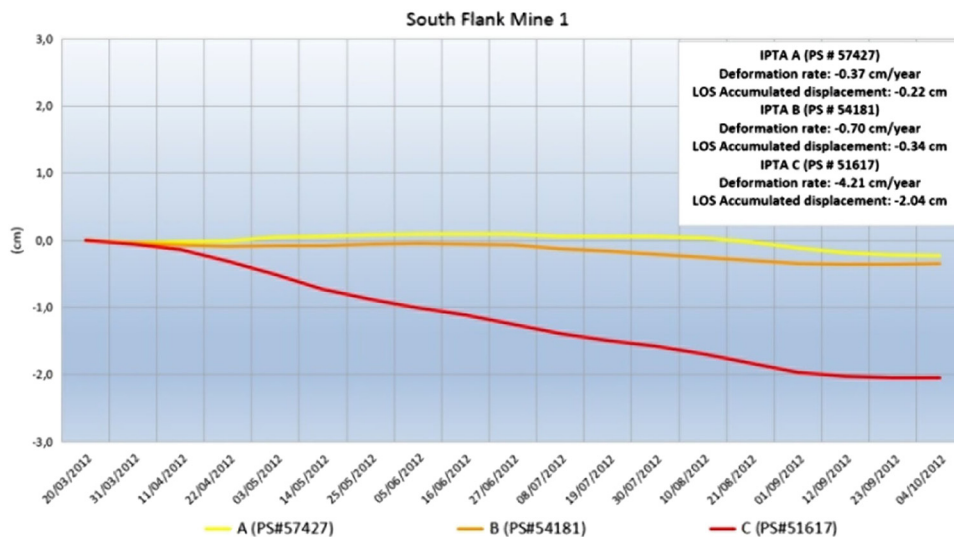


Fig. 11 LOS-projected TSX-1 displacement profiles for three points (A, B, and C) located along the SSR look direction from the bottom to the top of monitored bench walls of mine 1 (south flank).

It is worth noting that the deformation rates provided by TSX-1 with LOS range lengthening (away from the satellite) along pit walls of the south flank and LOS range shortening (toward the satellite) along pit walls of the north flank suggest linear motion components aligned toward the center of mine 1. Furthermore, the small deformations that were measured in the field are aligned along the SSR LOS, roughly oriented in the N-S direction due to the viewing geometry acquisition of the ground-based radar. These displacements could represent the N-S component of the overall small slope movement trend toward the center of mine 1 for the south flank. Taking into account that the geotechnical evaluation carried out by Vale S.A. is conclusive regarding the absence of major instabilities in this mine sector that could lead to large-scale movement and eventual failure, the PS detected trend is interpreted as normal deformation responsive to the open pit mining operations, characterized by stress relaxation of slopes due to pit excavation and the confinement provided by the rock mass that has been lifted.

6 Conclusions

In this paper, 33 TSX-1 images covering the period of March 2012 up to April 2013, divided in two data stacks for dry and wet seasons, were explored for monitoring surface displacements in the Azul manganese mine. IPTA results showed that most of the mining area was stable during the time span of the TSX-1 coverage. Ground displacement indicative of subsidence was measured over a waste dump, and it was interpreted as expected settlements with no additional evidences of pile instability. Ground displacements were also detected for benches along the northern and southern flanks of mine 1, with movements toward and away from the satellite, respectively. The intensity of the displacements was higher for the northern flank, which is located within a kilometer-scale structural corridor, characterized by folds, fractures, and faults oriented to WNW-ESE, with kinematics associated with dextral and sinistral components of the Carajás fault system. The displacements for both flanks are indicative of a general sense of movement toward the center of the pit during the TSX-1 coverage, probably caused by mining activities (unloading responses). Although it was not possible to directly compare the total amount of displacements measured by TSX-1 and SSR, the results showed concordance regarding the presence of small movements along the cut slopes for almost the same location. PSI data have provided a synoptic and detailed view of the deformation process affecting the mining complex. Since the technique depends on the sequential acquisitions, the information is not real time, and a complementary and synergistic use of PSI with field monitoring information is recommended for operational perspective. The PSI approach, providing data with high accuracy of displacements, over a dense grid and a large area, can be used for long-term monitoring and predictive solutions for in-pit mining operations, waste piles, and other mining structures without the need for ground instrumentations and fieldwork. In order to fully exploit the potentiality of PSI, the usage of ascending and descending SAR passes is necessary to complement the viewing geometry, to minimize the lack of information in the case of satellite acquisition failures, and also to get vertical and horizontal (only in E-W direction) deformation components.

Acknowledgments

This investigation was carried out under the scope of the FAPESP-Vale-INPE project (Process No. 2010/51267-9). The authors would like to thank Vale S.A. for providing access to geological, geomechanical, and *in situ* ground deformation data (slope stability radar). The National Council for Scientific and Technological Development (CNPq) is also acknowledged for grants received by the first and second authors during this investigation. The authors are particularly grateful to Dr. Charles Werner and Dr. U. Wegmüller for valuable suggestions on the use of GAMMA software and to the Geotechnical Vale's team in Carajás for the support during the field work.

References

1. S. A. Vale, "3Q15 production report," http://www.vale.com/EN/investors/information-market/quarterly-results/QuarterlyResultsDocs/PREPORT3T15_i.pdf (19 October 2015).

2. A. Vaziri, L. Moore, and H. Ali, "Monitoring systems for warning impending failures in slopes and open pit mines," *Nat. Hazards* **55**, 501–512 (2010).
3. GroundProbe, "The slope stability radar (SSR): ground breaking making mining safer," May 2014, <http://www.groundprobe.com/> (26 June 2014).
4. A. S. Nader, "Slope monitoring through slope stability radar as a key performance indicator of geotechnical development integrated with primary activities of mineral value chain," PhD Thesis, Politechnical Scholl, São Paulo University (2012) (original in Portuguese).
5. A. Ferretti, C. Prati, and F. Rocca, "Nonlinear subsidence rate estimation using permanent scatterers in differential SAR interferometry," *IEEE Trans. Geosci. Remote Sens.* **38**(5), 2202–2212 (2000).
6. A. Ferretti, C. Prati, and F. Rocca, "Permanent scatterers in SAR interferometry," *IEEE Trans. Geosci. Remote Sens.* **39**(1), 8–20 (2001).
7. C. Colesanti et al., "Detection of mining related ground instabilities using the Permanent Scatterers technique: a case study in the east of France," *Int. J. Remote Sens.* **26**(1), 201–207 (2005).
8. H. C. Jung et al., "Satellite observation of coal mining subsidence by persistent scatterer analysis," *Eng. Geol.* **92**, 1–13 (2007).
9. E. Biescas et al., "Two radar interferometric approaches to monitor slow and fast land deformation," *J. Surv. Eng.* **133**, 66–71 (2007).
10. G. Herrera et al., "Advanced DInSAR analysis on mining areas: La Union case study (Murcia, SE Spain)," *Eng. Geol.* **90**, 148–159 (2007).
11. Y. Guéguen et al., "Monitoring residual mining subsidence of Nord/Pas-de-Calais coal basin from differential and persistent scatterer interferometry (northern France)," *J. Appl. Geophys.* **69**, 24–34 (2009).
12. Z. Perski et al., "InSAR analyses of terrain deformation near the Wieliczka Salt Mine, Poland," *Eng. Geol.* **106**, 58–67 (2009).
13. D. Raucoles et al., "Validation and intercomparison of persistent scatterers interferometry: PSIC4 project results," *J. Appl. Geophys.* **68**, 335–347 (2009).
14. A.-H. M. Ng et al., "Mapping accumulated mine subsidence using small stack of SAR differential interferograms in the southern coalfield of New South Wales, Australia," *Eng. Geol.* **115**, 1–15 (2010).
15. U. Wegmüller et al., "Nonuniform ground motion monitoring with TerraSAR-X persistent scatterer interferometry," *IEEE Trans. Geosci. Remote Sens.* **48**(2), 895–904 (2010).
16. L. Jiang et al., "Potential of small-baseline SAR interferometry for monitoring land subsidence related to underground coal fires: Wuda (northern China) case study," *Remote Sens. Environ.* **115**, 257–268 (2011).
17. U. Wegmüller et al., "Monitoring mining induced ground-movements using SAR interferometric techniques," presented at *Proc. of Envisat Symp., 23–27 April 2007*, ESA, Montreaux, Switzerland, SP-636 (2007).
18. T. Woldai, G. Oppliger, and J. Taranik, "Monitoring dewatering induced subsidence and fault reactivation using interferometric synthetic aperture radar," *Int. J. Remote Sens.* **30**(6), 1503–1519 (2009).
19. G. Herrera et al., "Mapping ground movements in open pit mining areas using differential SAR interferometry," *Int. J. Rock Mech. Min. Sci.* **47**, 1114–1125 (2010).
20. M. E. Hartwig, W. R. Paradella, and J. C. Mura, "Detection and monitoring of surface motions in active open pit iron mine in the Amazon region; using persistent scatterer interferometry with TerraSAR-X satellite data," *Remote Sens.* **5**, 4719–4734 (2013).
21. J. C. Mura et al., "Monitoring of surface deformation in open pit mine using DInSAR time-series: a case study in the N5W iron mine (Carajás, Brazil) using TerraSAR-X data," *Proc. SPIE* **9243**, 924311 (2014).
22. W. R. Paradella et al., "Mapping surface deformation in open pit iron mines of Carajás province (Amazon region) using an integrated SAR analysis," *Eng. Geol.* **193**, 61–78 (2015).
23. W. R. Paradella et al., "Complementary use of information from space-based DInSAR and field measuring systems for operational monitoring purposes in open pit iron mines of

- Carajás mining complex (Brazilian Amazon region),” *Int. Arch. Photogramm. Remote Sens. Spatial Inf. Sci.* **XL-7/W3**, 905–911 (2015).
24. A. C. R. Nogueira, “Análise faciológica e aspectos estruturais da Formação Águas Claras, Região Central da Serra dos Carajás, Pará,” PhD Thesis, Federal Pará University (1995).
 25. M. L. Costa, O. J. C. Fernandez, and M. E. R. Requelme, “The Azul Mn deposit, Carajás: stratigraphy, mineralogy, geochemical and geological evolution,” in *Characterization of the Mineral deposits in Mineral Districts of the Amazonia*, pp. 231–333, Carajás, Brazil, internal report (2005).
 26. R. V. L. Pinheiro, “Reactivation history of the Carajás and Cinzento Strike-Slip Systems,” PhD Thesis, University of Durham, UK, Amazon Brazil (1997).
 27. D. C. C. Silva, “Estudo da geometria e cinemática das rochas sedimentares arqueanas da mina do Igarapé do Azul, Carajás, Pa,” MSc Thesis, Federal University of Pará (2006).
 28. S. A. Vale, “Lithostructural and lithogeomechanical mapping of mine 1, Azul Mn mine,” Vale, Carajás, Brazil, internal report (2012).
 29. Z. T. Bieniawski, *Engineering Rock Mass Classifications*, p. 272, John Wiley & Sons, New York (1989).
 30. W. R. Paradella and P. Cheng, “Using GeoEye-1 stereo data in mining application: automatic DEM generation,” *Geoinformatics*, V. 10–12 (2013).
 31. S. A. Vale, “Geotechnical monitoring with slope stability radar: central-north and south walls, mine 1, Azul Mn mine,” Vale, Carajás, Brazil, internal report (2012).
 32. P. Berardino et al., “A new algorithm for surface deformation monitoring based on small baseline differential interferograms,” *IEEE Trans. Geosci. Remote Sens.* **40**, 2375–2383 (2002).
 33. M. Costantini, “A novel phase unwrapping method based on network programming,” *IEEE Trans. Geosci. Remote Sens.* **36**(3), 813–831 (1998).
 34. A. Ferretti, C. Prati, and F. Rocca, “Permanent scatterers in SAR interferometry,” *IEEE Trans. Geosci. Remote Sens.* **39**(1), 8–20 (2001).
 35. C. Werner et al., “Interferometric point target analysis for deformation mapping,” in *Proc. IGARSS*, pp. 4362–4364 (2003).
 36. GAMMA Remote Sensing, “User’s guide version 1.4,” in *GAMMA Remote Sensing and Consulting AG*, Bern, Switzerland (2013).
 37. M. Orman, R. Peevers, and K. Sample, “Waste piles and dumps,” in *SME Mining Engineering Handbook*, P. Darling, Ed., 3rd ed., Vol. 1, pp. 667–680, Society for Mining, Metallurgy and Explorations, Englewood, CO (2011).
 38. A. Jarosz and H. Zahiri, “Interferometric synthetic aperture radar (InSAR) and its potential to monitor subsidence over caving zones induced by underground mining,” in *First Int. Future Mining Conf. & Exhibition 2008*, pp. 143–149 (2008).

Carolina de Athayde Pinto is a geologist. She received her BS degree in geology from the University of Campinas, Brazil, in 2012, and her MS in remote sensing from the National Institute for Space Research (INPE, Brazil) in 2015. Her research interests include remote sensing, image processing, image classification, synthetic aperture radar (SAR), InSAR, DInSAR, persistent scatterers, especially with application to change detection.

Waldir Renato Paradella is a geologist with a BS in geology from the University of São Paulo (USP), Brazil, in 1973, MS in remote sensing from INPE in 1976, and PhD in geology from USP in 1983. Since 1974, he has been with INPE and currently is a senior researcher. (In 1988 and 1995, he was with CCRS, Canada, as a postdoctoral fellow and visiting scientist). His main research interests include geoscience applications in tropical environments with SAR.

José Claudio Mura received his BS degree in electric engineering from the USP at São Carlos School of Engineering (EESC-USP, Brazil) in 1978, his MS degree in electronics and telecommunications from the Aeronautics Institute of Technology, Brazil, in 1985, and his PhD in applied computer science from INPE in 2000. He has been with INPE since 1979, and his current research interests include SAR image processing, SAR polarimetry, InSAR, and DInSAR.

Fabio Furlan Gama received his BS degree in electrical engineering from Valeparaibano Education Foundation, Brazil, in 1986 and his PhD in remote sensing in 2007 from INPE. He works at INPE in the development of systems and remote sensing applications by radar, and as assistant professor in the postgraduate course in remote sensing. His research interests include SAR interferometry, differential SAR interferometry, SAR polarimetry, and applications of SAR surveying for land use/cover.

Athos Ribeiro dos Santos received his BS degree in geology from São Paulo State University (UNESP), Brazil, in 1973, his MS degree in remote sensing from INPE in 1977, and his PhD in geology from USP in 1986. He has been with INPE since 1974. His main research interests include geological applications in tropical environments with SAR.

Guilherme Gregório Silva is an environmental engineer. He received his BS degree in environmental engineering from the University of Paraíba Valley, Brazil, in 2010, and currently, he is an MS student in remote sensing at INPE. His research interests include environmental, cartography, geodesy, remote sensing, GIS, classification, SAR, InSAR, DInSAR, and PSInSAR.

Marcos Eduardo Hartwig received his BS degree in geology from UNESP, Brazil, in 2003, his MS degree in geosciences from USP in 2006, and his PhD in remote sensing from INPE in 2014. His main research interests include the use of remote sensing (optical and radar) applied to geosciences, and geological and geotechnical applications in tropical environments.